Received: 8 April 2022 | Revised: 1 October 2022 | Accepted: 23 June 2023

DOI: 10.1002/we.2855

RESEARCH ARTICLE

WILEY

The flow in the induction and entrance regions of lab-scale wind farms

Magnus K. Vinnes[1] | Nicholas A. Worth[1] | Antonio Segalini[2] | R. Jason Hearst[1]

[1]Department of Energy and Process Engineering, Norwegian University of Science and Technology, Trondheim, Norway

[2]Department of Earth Sciences, Uppsala University, Uppsala, Sweden

Correspondence
R. Jason Hearst, Department of Energy and Process Engineering, Norwegian University of Science and Technology, Trondheim, Norway.
Email: jason.hearst@ntnu.no

Funding information
STandUP for Wind

Abstract

With the increasing demand for wind energy, it is important to be able to understand and predict the available wind resources. To that end, the present wind tunnel study addresses the flow in the induction and entrance region of wind farms through particle image velocimetry, with focus on differences between actuator disks and two-bladed rotating wind turbine models. Both staggered and aligned farm layouts are examined for three different incoming wind directions. For each layout, 69 disks or turbines are used, and the field of view ranges from 12 rotor diameters upstream of the farms to 8 diameters downstream of the first row. The results show that the induction, or blockage effect, is higher for the disks, even though the thrust (or drag) coefficient is the same. In contrast, the wake is stronger downstream of the turbines. The orientation and layout of the farm do not have a major impact on the results. Modal decomposition of the flow shows that the flow structure similarity between the disk and turbines improves downstream of the second row of wake generating objects, indicating that the substitution of wind turbines by actuator disks is more appropriate for wind farms than for the investigation of single wakes.

KEYWORDS
actuator disk, wind farm, wind farm blockage, wind tunnel experiments, wind turbine

1 | INTRODUCTION

In classical momentum theory, a wind turbine is modeled as a pressure drop,[1] often called an actuator disk (AD). In this way, the induction region and wake region that are typical of the interaction between flow and turbine are modeled. Due to relatively simple implementation and reduced computational costs, it is still common to use the AD methodology in simulations, in particular when modeling a wind farm consisting of multiple turbines (e.g., previous studies[2–5]).

It is similarly possible to simplify experiments by using static porous disks as wind turbine models, which represent the experimental equivalent to ADs. Thus, here porous disks will also be referred to as ADs. Single ADs have been used to study wake meandering,[6,7] the wake of a yawed turbine,[8] the effect of transient loads,[9] the effect of the boundary layer on the wake,[10] and, recently, the effect of inertial particles on the turbulent wake.[11] However, the major benefit comes when studying a wind farm with multiple turbines. As such, ADs have been used to measure the power output of a wind farm through drag measurements[12] and the power output through strain gages on the individual turbines in a farm.[13]

There are scaling challenges when using miniature wind turbines, for example, it is not possible to maintain both the same tip speed ratio and Reynolds number seen for utility-scale turbines. However, the disadvantages are compensated by the possibility to measure large flow fields compared to the turbine, as well as the possibility to control the incoming flow. Lab-scale experiments are still commonly used (e.g., previous studies[12–18]) and are needed to improve the understanding of wind turbine and wind farm flow physics and to be used as calibration and verification of numerical models.[19]

The near wake of a wind turbine is a complex flow. It is highly three dimensional, consisting of tip and root vortices that are transported downstream forming helical structures and asymmetric wake profiles.[14,19,20] Many of these flow phenomena cannot be replicated by a static AD. After some distance, in a transition region, the vortices break down. The flow in the far wake is not so greatly influenced by the turbine specific features, but rather determined by global features as the thrust coefficient (C_T), power coefficient, and the incoming flow.[19] The far wake begins somewhere between 2 and 4 rotor diameters (D) downstream of the turbine.[19] This is a shorter distance than the $5-10D$ spacing between turbines in many commercial wind farms.[21] Thus, for many practical applications, it is not necessary to know the detailed features of the near wake, and the use of ADs can be justified.

In addition to the velocity deficit in the wake, momentum theory also predicts reduced velocity in the flow upstream of wind turbines. Through vortex theory, Medici et al.[22] demonstrated numerically and experimentally that an induction zone model based on a vortex approach reasonably predicts the flow upstream of three different lab-scale wind turbines. The applicability of the model has later been confirmed by wind tunnel measurements[14,23] and full-scale measurements.[23,24] Bastankhah and Porté-Agel[14] also showed a small asymmetry in the induction region of a wind turbine in a boundary layer. Based on RANS simulations, Troldborg and Meyer Forsting[25] developed a new analytical model of the wind turbine blockage, which yielded accurate results at distances more than $0.5D$ upstream of the turbine.

Many modern wind turbines are located in clusters and are affected by each other. The flow in and around a wind farm can be divided into the wind farm induction region, the entrance and development region, the fully developed region, the exit region, and the wind farm wake.[19] Through met-mast measurements and RANS simulations, Bleeg et al.[26] demonstrated that wind turbines in a farm are affected not only by the wakes of the turbines upstream but also by the combined induction of downstream turbines. As such, there is a global blockage reducing the available power in the wind. The findings have later been confirmed by field measurements performed by Schneemann et al.[27] They found a measurable effect under stably stratified ABL conditions but not in the unstable case. Later, Segalini and Dahlberg[17] investigated how the global blockage changed with the number of rows and with changing distance from the first row to the rest of the farm. Based on vortex theory, Branlard and Meyer Forsting[28] introduced a model to describe the wind farm flow, targeted to include the global induction in particular. They report only a small overestimation of the velocity in the induction region. Recently, Segalini[29] developed an analytical model for wind farm blockage, which agreed with RANS simulations.

In the entrance region of a wind farm, covering the first rows of turbines, the flow at turbine height is heterogeneous and dominated by wakes of individual turbines.[19] Chamorro and Porté-Agel showed that the tip vortices lose their strength moving downstream in the wind farm. In fact, the tip vortices shed by the second row of turbines are already weaker than those shed by the first row.[18] The transport of energy from the flow above a wind farm into the farm is important for the available energy and has been studied extensively (e.g., previous studies[18,30–34]). In the developed regions of a farm, the energy transport is dominated by turbulent fluctuations, while in the developing regions near the entrance of the farm, the mean vertical velocity is the driving factor.

Matching flow statistics around ADs and wind turbines, both for single wake generating objects (WGOs) and WGOs in wind farms, has received considerable attention in the literature. Examples of such validations in numerical simulations are found in previous studies.[35–39] Different studies have also compared AD wakes to wind turbine wakes experimentally. Aubrun et al.[40] investigated the wakes of an AD and a lab-scale wind turbine in both homogeneous isotropic turbulence and in a simulated atmospheric boundary layer (ABL). At $3D$ downstream of the WGOs, they found that the turbulent statistics up to the fourth moment matched between the WGOs. Also, in the work of Lignarolo et al.,[41] the mean wake profiles of a wind turbine and an AD agree well, although the turbulence intensity tends to be higher in the shear layer of the wind turbine wake compared to the AD wake. Furthermore, they demonstrated that the tip vortices lead to different transport mechanisms between the wake and the free-stream. Camp and Cal[42,43] experimentally compared the flow around a WGO in the fourth row of wind farms containing turbines and ADs. They found that the turbine yields higher turbulent stresses in the wake, higher turbulent production, and also higher vertical energy entrainment into the wake region. Both one-point and two-point statistics were found to match in the far wake centerline downstream of a turbine and porous disk by Neunaber et al.[44]

The aforementioned experimental studies use different AD designs. They can broadly be divided into ADs constructed of wire meshes (Aubrun et al.[40] and Lignarolo et al.[41]) and ADs with spars protruding from the center, held together by rings at different radial positions (Camp and Cal[42,43] and Neunaber et al.[44]). The differences in wakes of the different types have received some attention in the literature. Aubrun et al.[45] compared the wakes of two ADs with different designs, one wire mesh disk and the non-uniform disk of Camp and Cal,[42,43] measured in nine different facilities. The process of choosing a design for an AD that best acts as a static wind turbine model was highlighted by Helvig et al.[46] They ended up with a non-uniform design, similar to the Camp and Cal[42,43] disk and showed that it could reproduce the mean features of the wake satisfactorily but that the instantaneous structures in the wake differed significantly. Recently, Vinnes et al.[21] compared the far wake of two ADs, one from each of the design principles. Their results highlight the importance of carefully choosing the AD design, as even the mean velocity

profiles of the two disks differ in the far wake, and the governing physics of the wakes are different. Neither of the disks could reproduce the asymmetry in a wind turbine wake.

To date, no studies have investigated the induction region of an AD experimentally or explicitly compared the induction region of rotating turbines with ADs. Camp and Cal[42,43] measured the flow upstream of an AD and a wind turbine, but those measurements were taken inside a wind farm such that the flow was dominated by the wakes of upstream WGOs. Their studies are also the only ones comparing ADs to rotating turbines in wind farms experimentally.

This study compares both the induction region and the beginning of the entrance region of wind farms modeled by ADs and wind turbines. The entrance region is separated into the wake region downstream of the first and second rows of WGOs and the entrainment region above the same rows. Measurements were performed with particle image velocimetry (PIV), such that full flow fields can be evaluated. The field of view ranges from 12D upstream of the farm to 8D downstream of the leading row, as well as from the ground up to 2.6D above the top tip of the WGOs. Both aligned and staggered farm layouts are evaluated, with three different incoming wind directions, yielding a total of 12 flow cases. Although the induction is important for the wind farm production, the flow in this region of a wind farm has not previously been compared between ADs and rotating wind turbine models. The significance here is to shed light on the impact of the AD simplification on the conclusions drawn from the induction and entrance regions of a wind farm.

2 | EXPERIMENTAL PROCEDURE

Two-bladed, freely rotating models were used as wind turbines in this study. While three-bladed turbines are the most common at utility scale, several earlier studies have also employed two-bladed models.[22,41,47–49] Furthermore, the specific turbines used in the current study have been used in numerous previous studies.[17,18,46,50] The mean velocities in the wake are not significantly altered when comparing two- and three-bladed rotors,[51,52] and existing analytical formulae provide relationships that agree reasonably well with both two- and three-bladed rotors.[28,29,53] Thus, for the purpose of this study, two-bladed models are acceptable. The turbine models have a C_T of 0.57,[46] a diameter of $D = 45$ mm, and they are mounted to a tower with a hub height of $h = 65$ mm. It should be noted that the measured C_T was averaged over several turbines. The tip speed ratio of the models is approximately 5.[17] However, the rotational speed of the turbines was not controlled in Helvig et al[46] or in the present study, so there might be differences in thrust and rotational speed between the individual turbines due to different friction. For more details on the turbines, see earlier works.[17,18,46,50] A front view of the model wind turbine is shown in Figure 1A.

The ADs are non-uniform porous disks with decreasing blockage with increasing distance from the center. They have $C_T = 0.56$,[46] $D = 45$ mm, and were mounted to towers similar to the wind turbine towers. Helvig et al.[46] found that this particular disk design produced the flow field that best matched the flow around the rotating models. They showed that the mean velocity statistics of the wakes of this AD and the turbines used here match reasonably well, although the instantaneous structures differ due to the tip vortices in the wind turbine wake. The design is the NHD35 disk in that work. A schematic of the AD is shown in Figure 1B.

For both the ADs and the wind turbine models, six different wind farm layouts were investigated. To approximate a wind farm of infinite size, a total of 69 WGOs were used in each layout. Preliminary measurements of the induction region showed little dependence on the size of the wind farm. The different layouts are shown in Figure 2. The top row shows an aligned farm, positioned at three different angles relative to the incoming flow. These cases are named A0, A15, and A30 for 0°, 15°, and 30° rotation of the farm, respectively. In the same way, the bottom row shows a

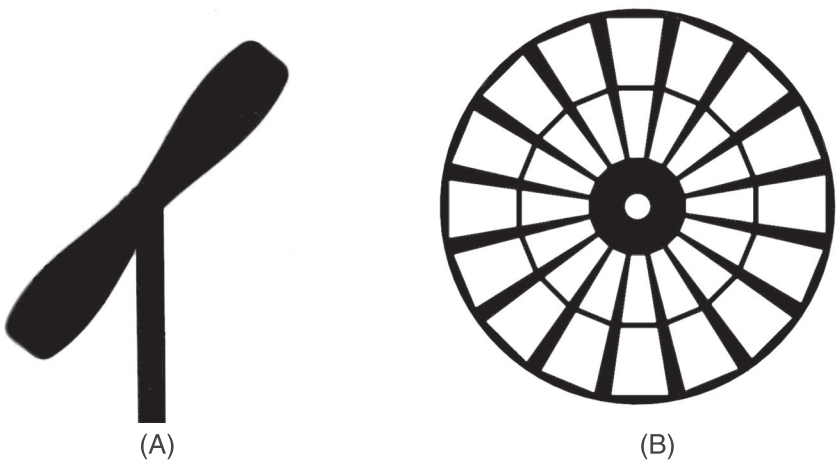

FIGURE 1 Schematics of (A) the model wind turbine and (B) the actuator disk used in the present work.

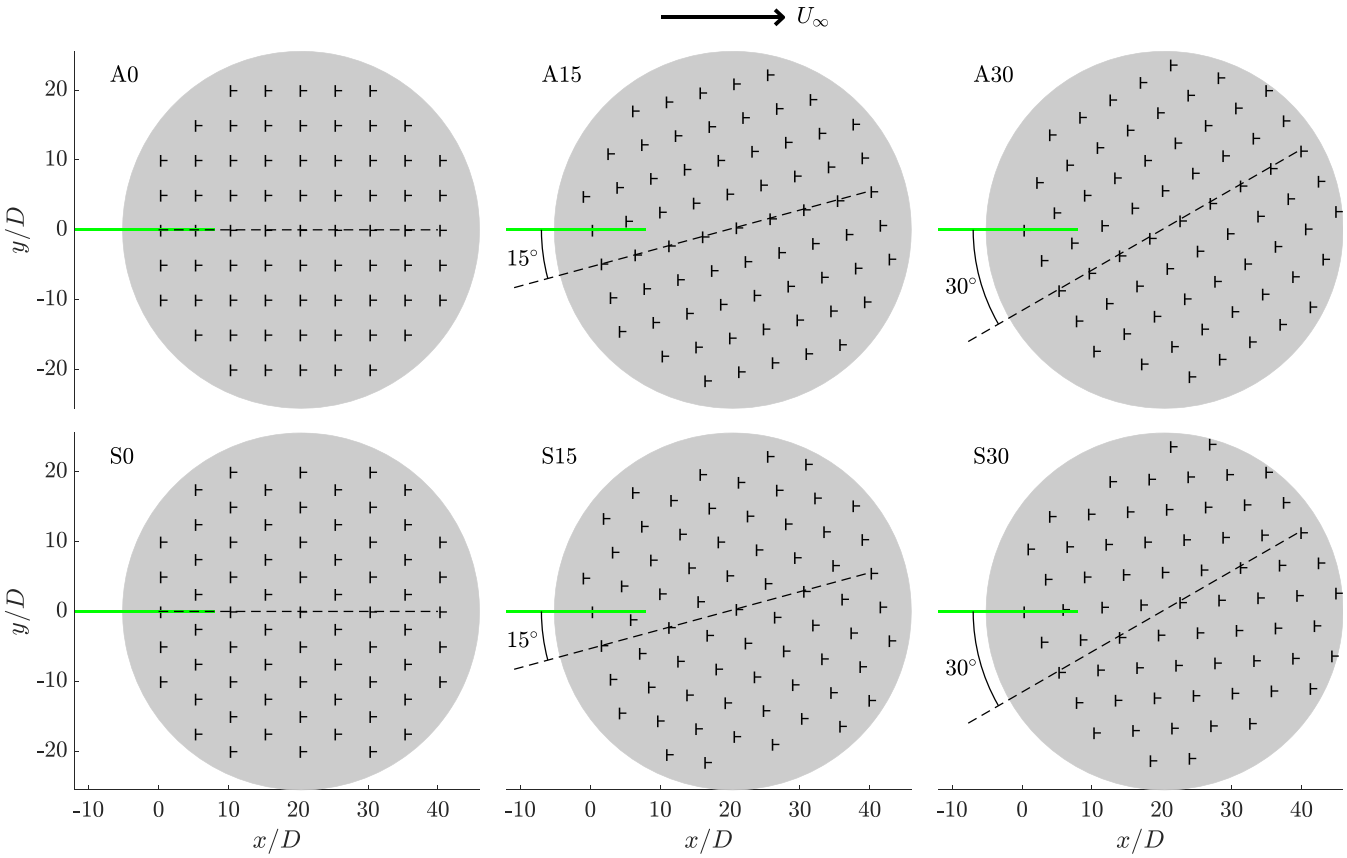

FIGURE 2 The six different layouts used in the current experimental campaign. The green line shows the extent of the field of view, while the dashed line illustrates the spanwise centerline of the aligned and staggered farms. The gray circle represents the steel plate the wake generating objects were mounted to.

staggered farm at the same angles, with naming convention S0, S15, and S30. For turbines and disks, a T or a D is added in front, such that, for example, TA0 is the aligned turbine case at 0° rotation. Note that the WGOs were yawed such that they always face the incoming flow, and that one of the disks or turbines in the leading row was kept at the same physical position relative to the data acquisition cameras for comparison. This WGO is the object farthest to the left of the illuminated plane (shown in green) for each layout in Figure 2 and will be referred to as the leading WGO. The spacing between the WGOs was $S = 5D$ in both directions, and for the staggered cases, every other row was shifted by $S/2 = 2.5D$. The disks and turbines were mounted by magnets to a circular steel plate positioned on the wind tunnel floor, as illustrated by the gray circles in Figure 2. This led to a small step (3 mm) approximately $6D$ upstream of the leading WGO.

The measurements were done in the large, recirculating wind tunnel at the Norwegian University of Science and Technology (NTNU). It has a closed test section with a length of 11.15 m and a width of 2.71 m. The height of the test section increases gradually from 1.8 to 1.85 m to compensate for the growing boundary layers along the test section and ensure that the pressure gradient is zero in the streamwise direction with an empty test section. The leading WGO is located $37D$ downstream of the entrance of the test section.

The origin of the coordinate system is set to the center of the leading WGO as indicated in the sketch in Figure 3, with x being the streamwise component and z the vertical component. In any figure plotted with the vertical axis, the right side also shows the $\tilde{z}$ coordinates, which is the vertical coordinate with the zero position at the steel plate.

Two-dimensional, two-component PIV was used for collecting the velocity fields. To evaluate the effect the induction region has on a turbine, the measurement plane was spanwise centered at the location of the leading WGO. The total field consists of four separate PIV fields, each with dimensions $4.6D \times 6.8D$ (height $\times$ width). Two LaVision Imager LX Pro 16 Mpx cameras were positioned outside the plexiglass wall of the wind tunnel. The flow was illuminated by a Litron L200-15, Nd-YAG dual-pulse laser, with a wavelength of 532 nm and a measured power of 208 mJ per pulse. A set of spherical and cylindrical lenses were used to create a thin laser sheet. The laser and lenses were positioned above the tunnel, and light was directed into the tunnel through a plexiglass roof. After acquiring the two upstream fields (shown in dark green in Figure 3) for all the experimental cases, the cameras and laser were moved downstream to capture the two remaining fields (light green in Figure 3). The wind tunnel was seeded by a Martin Magnum 2500 Hz smoke machine using the Martin Rush & Thrill Haze Fluid, yielding particles with a size of approximately 1 μm. For each test case, approximately 1000 image pairs were obtained. Tests show that the mean velocity converges to $\pm 0.5\%$

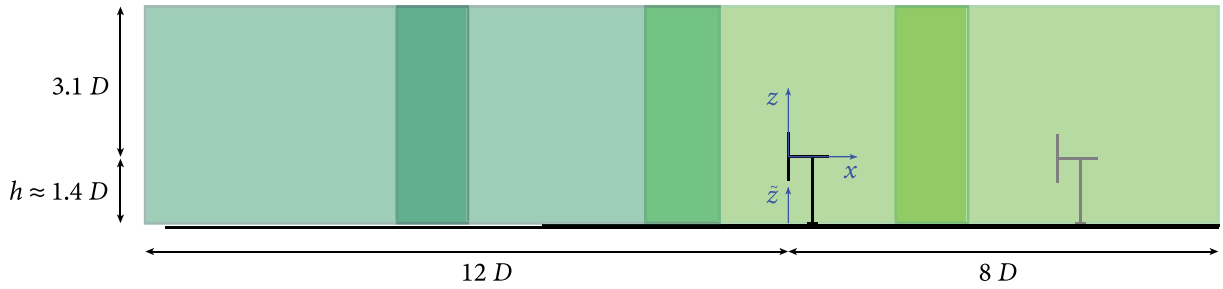

FIGURE 3 Schematics of the experimental setup. The two dark green fields were captured for all experimental cases, before the cameras and laser were moved downstream to capture the two light green fields. The second wake generating object, colored light gray, is included from the aligned, 0° case, but the position will vary with the different layouts, whereas the first object is always at the same spot.

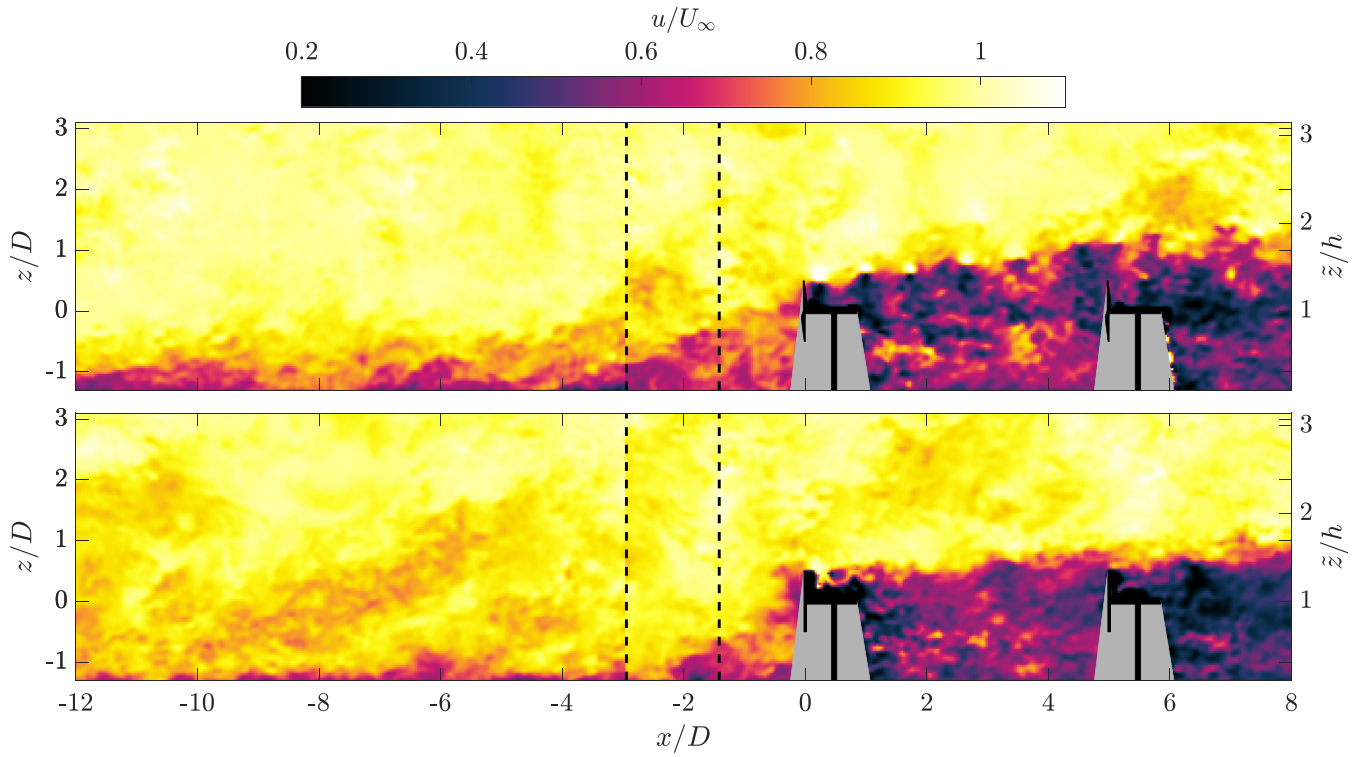

FIGURE 4 Instantaneous velocity fields for the TA0 (top) and DA0 (bottom) cases. The dashed lines show where the upstream and downstream instantaneous fields, acquired separately, overlap. The downstream field is shown in the overlap.

after 500 image pairs. Only the center of the wake converges slower but still within $\pm 1\%$ after 500 frames. The sampling frequency was 0.6 Hz ensuring that each instantaneous vector field is statistically independent. Both the cameras and the laser were controlled through a LaVision programmable timing unit (PTU-X) by LaVision DaVis 8.

The images were pre-processed to reduce noise before PIV calculations were performed over three passes with a final window size of 48×48 px and a window overlap of 50%. Each of the four fields of view then contained 204×137 (height $\times$ width) vectors. All further processing was done in Matlab. For the sets of fields acquired simultaneously, a stitching algorithm was applied for every instantaneous pair of vector fields. Figure 4 shows examples of the stitched fields for the TA0 and DA0 cases. The dashed lines indicate where the two independent sets of fields overlap such that stitching of instantaneous fields is impossible. Instead, the same stitching algorithm was used on the calculated mean statistics to achieve the final full field of view. In the final stitching of the means, the variables were normalized by the free-stream velocity U_∞. The two sets of velocity vectors were also corrected to each other by a factor determined by the mean velocity in a defined window in the overlapping region between the fields of view. This correction factor did not exceed 0.8% for any of the experimental cases. After removing the outermost vectors of the total field, the final field of view is 590×133 vectors, covering approximately $-12 \le x/D \le 8$ and $-1.4 \le z/D \le 3.1$ (or $0 \le \tilde{z}/h \le 3.1$). The vector spacing was $0.034D$ in both directions.

U_∞ was measured by a Pitot tube mounted to the roof of the tunnel above the farm. The top tip of the WGOs reached just above 5% of the wind tunnel height. If the wind farm frontal area is considered as as a solid box, the open area on both sides of the farm ensures that the blockage of the tunnel is well below 5%, such that confinement effects on the measured U_∞ should be negligible.[54] This was also checked by measuring the free-stream velocity over farms with different number of turbines, and no measurable effect on U_∞ was found. Throughout the campaign, U_∞ was kept at 6.35 ± 0.04 m/s, yielding a Reynolds number based on D and the free-stream velocity of $Re_\infty = U_\infty D/\nu = 18,500 \pm 200$. The Reynolds number based on the velocity at the hub of the leading turbine/AD, measured without any WGOs in the tunnel, was $Re_{hub} = U_{hub} D/\nu = 17,200$.

Figure 5 shows the undisturbed velocity profiles, acquired without any WGOs but with the steel mounting plate in the tunnel. The profiles are averaged over five vectors in the streamwise direction. The same averaging procedure is used for all vertical profiles presented in this paper. For the streamwise profiles, the same averaging of five vector rows is done in the vertical direction. In addition, they are smoothed with a nine-vector moving average in the streamwise direction. The profiles in Figure 5 are typical examples of an evolving boundary layer. The turbulence intensity, defined as u'/U, with u' being the root mean square of the streamwise velocity fluctuations u, and U denoting the mean velocity, is approximately 7%. This is in the lower end of the recordings at GROWIAN, where the turbulence intensity typically was in the range from 5% to 15%.[55] However, lower turbulence enables the differences in the governing physics between the turbines and ADs to be more readily observed.

3 | RESULTS

3.1 | Induction region

Vertical profiles of the streamwise velocity are shown for all experimental cases at different streamwise positions in Figure 6. At 10D upstream of the leading WGO, there is already a small induction effect present. This increases gradually when the distance to the farm is reduced. Far upstream, the induction has the same magnitude throughout the measurement domain, such that the velocity profiles are similar to the undisturbed boundary layer case but with a smaller magnitude. In this region, the induction is mainly an effect of the global wind farm induction. Starting at 1D upstream, the induction is noticeably higher in proximity to the WGO, indicated with dotted lines. Here, the local induction of the single turbine starts affecting the flow more. In this region, the induction of the disks and turbines are distinguishable. The induction upstream of the AD farms is noticeably higher than that of the turbine farms. It is interesting to note that the layout of the farm does not seem to affect the induction, while there is a significant difference between the induction upstream of the two different WGOs. Figure 7 shows the vertical velocity profiles at the same streamwise positions. Starting around 5D upstream of the farms, there is increased upward flow compared to the clean boundary layer case. The velocity magnitude difference grows approaching the farms. The added vertical velocity is more prominent in the top part of the measurement domain. If the horizontal velocity inside the farm is treated as small, the vertical velocity is an integrated effect of all the induction below a certain height. Hence, the higher level of vertical velocity in the top of the measurement domain agrees with the measured induction. For the two profiles measured closest to the WGOs, the vertical velocity is directed outwards from the center of the WGO. The upward velocity upstream of the top half of the WGOs has a higher magnitude than the corresponding downward velocity upstream of the bottom half. This arises from the integrated upward velocity seen already at $x/D = -5$ and the floor blocking the flow from being directed downwards. The magnitude, both upward and downward, is higher for the disk cases, consistent with the profiles in Figure 6. Just above the floor, at

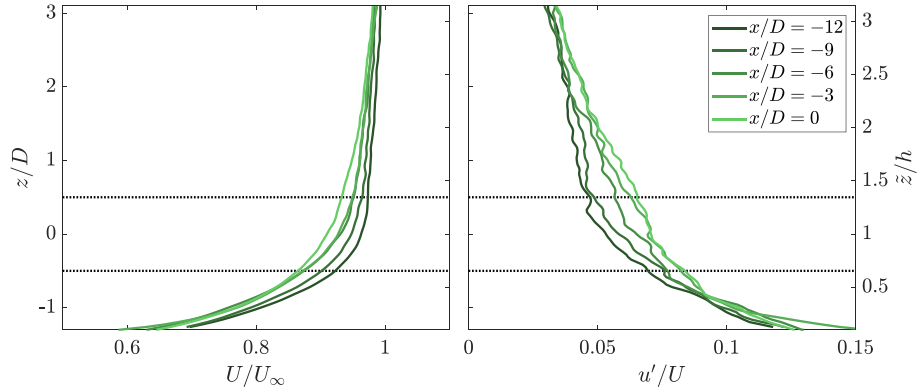

FIGURE 5 Profiles of the undisturbed boundary layer velocity (left) and turbulence intensity (right) measured at different positions in the clean configuration. The dotted lines mark the top and bottom tip positions of the WGOs.

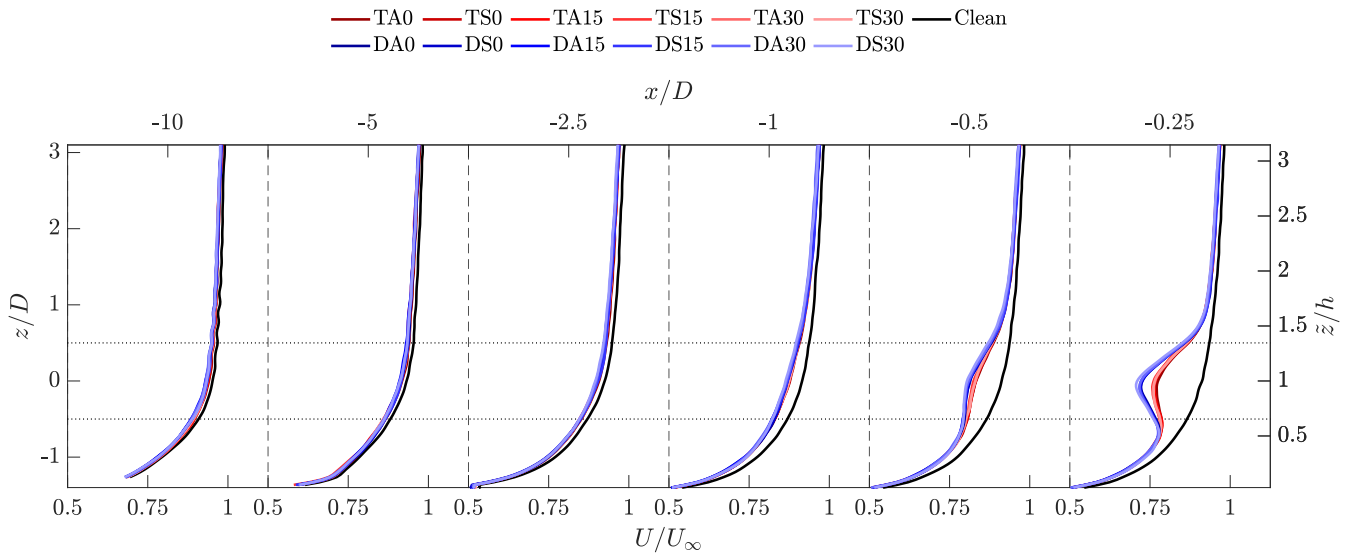

FIGURE 6 Vertical streamwise velocity profiles in the induction region of the farm.

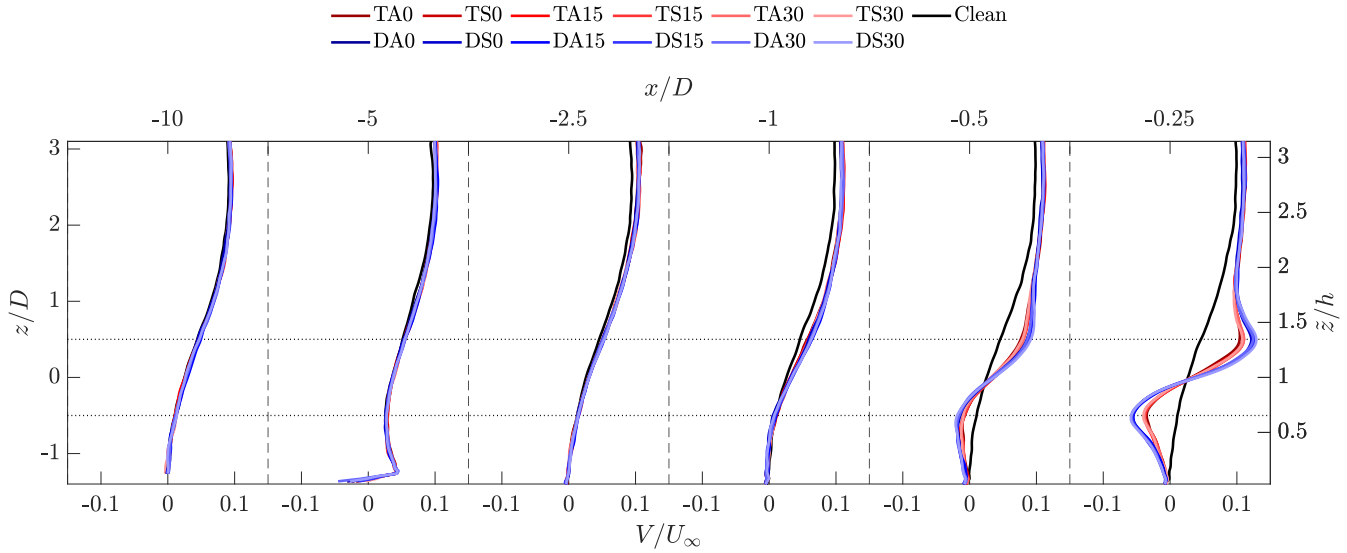

FIGURE 7 Profiles of the vertical velocity in the induction region of the farm.

$x/D = -5$, the magnitude of vertical velocity suddenly increases. This is just downstream of the small step (3 mm) onto the steel plate, and it is the same for all farm cases and the clean flow. It is not visible closer to the farm, and does not affect the reported results.

A clearer view on the streamwise evolution of the induction can be obtained by looking at the streamwise velocity profiles at hub height, shown in Figure 8. As far as 12*D* upstream of the farm, the streamwise velocity is reduced by 1% to 2% just by the presence of the farm. It seems like the disks have a slightly higher induction this far upstream, but these differences are within the measurement uncertainties (0.5% of U_∞, based on the uncertainty in the velocities measured by the Pitot tube and the PIV). Just upstream of the AD, the measured induction is 20% whereas it is 15% upstream of the turbine, which shows a significant difference despite the similar drag of the two WGOs. This is surprising, as it contradicts the direct relationship between thrust and induction in the linear momentum theory. However, the velocity at hub height has the maximum difference, and the measurements do not tell us anything about the out-of-plane induction, such that the total induction over the WGO swept area is unknown and might be more equal.

While Figure 8 shows the induction at hub height, it does not give information about how the velocity reduction is distributed over the height of the WGOs. To obtain that information, the axial induction factor a can be used. In linear momentum theory, it is defined as the difference between the free-stream velocity far upstream and the velocity crossing the AD, normalized by the free-stream velocity, that is, $a = (U_\infty - U_{\text{disk}})/U_\infty$. This definition does not account for the non-uniform velocity profile and vertical velocity in the evolving boundary layer.

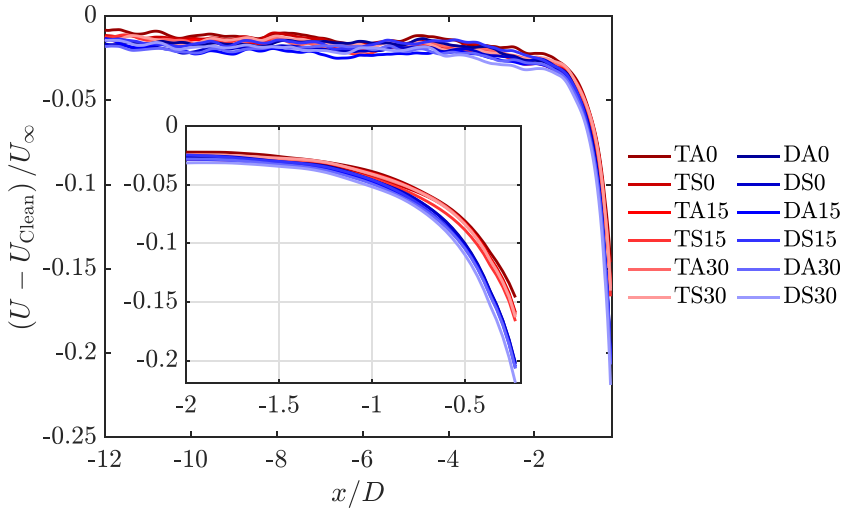

FIGURE 8 Streamwise velocity distribution at hub height. The inset provides a close-up of the region near the wake generating objects.

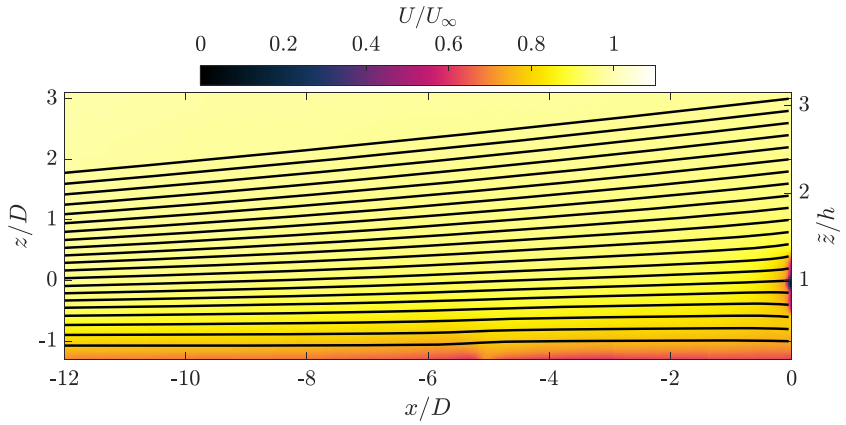

FIGURE 9 Mean streamwise velocity in the induction region for TA0. The streamlines are equidistant just upstream of the turbine.

The streamlines in Figure 9 illustrate the upward displacement of the flow. It is more relevant to calculate the induction of the flow hitting the WGO itself. Therefore, the induction factor used here, a^*, is calculated as the induction of the flow inside two streamlines, with the far upstream velocity U_0 being at $x/D = -12$ and taking U_{disk} just upstream of the disk, such that

$$a^* = (U_0 - U_{\text{disk}})/U_0. \tag{1}$$

The distribution is then found by calculating a^* between streamlines passing through every $0.1D$ at the WGO location. Note that for clarity only every other streamline used in the computations are shown in Figure 9. To also see the effect on the surrounding flow, Figure 10 shows a^* through most of the height of the measurement domain. To improve the readability of the following figures, only 0° cases are plotted. The analysis was done for all cases, and, as was observed for the velocity profiles, there are no significant differences between the different farm orientations.

Figure 10 confirms the higher induction upstream of the disks. Around the center of the WGO the difference is as high as $\Delta a^* = 0.035$, or 19% of the AD induction. This is to some extent compensated by a higher induction above the turbines, in particular in the region around $z/D = 1$. Again, this induction is only for the spanwise center of the WGO, and the current data does not reveal the extent of the induction in the out-of-plane direction. In particular, the rotational effect of the turbine leads to asymmetries in the induction.[14] Even though it seems like the total induction is higher for the disk, it might be partly or fully compensated by the induction over the total rotor/disk area. Nevertheless, it is clear that the induction, or at least the induction distribution, differs between the AD and turbine. Still, the difference is not as large for the global wind farm induction.

The recently developed wind farm blockage model by Segalini[29] is a simple linearized model based on superposition of the induction of individual turbines. It reads

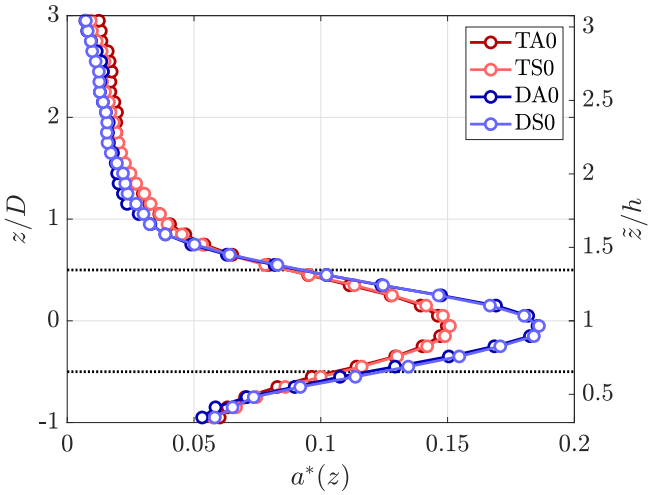

FIGURE 10 Distribution of the modified induction factor a^* (see Equation 1). The vertical coordinate corresponds to the mid-point between two streamlines just upstream of the WGO.

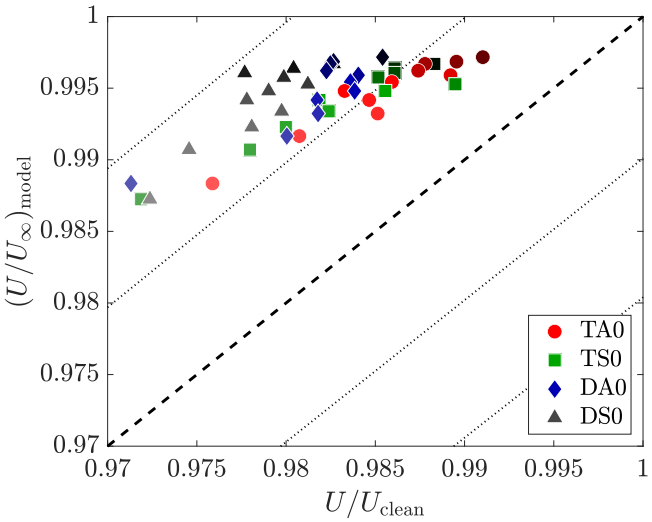

FIGURE 11 Comparison of experimental data to the model proposed by Segalini.[29] The experimental data are taken at hub height. Colors range from dark at $x/D = -12$ to light at $x/D = -2$. An average over a five by five vector window is calculated and used for each point in the scatter plot. Dotted lines indicate where the deviation is 1% and 2% of the undisturbed velocity.

$$\frac{U(\mathbf{x})}{U_\infty} = 1 + \sum_{n=1}^{N} \frac{\widetilde{C_T}(x - \xi_n)}{8|\mathbf{x} - \boldsymbol{\xi}_n|^3}, \tag{2}$$

where $\mathbf{x} = [x, y, z]$ and $\boldsymbol{\xi}_n$ is the position of turbine n, with ξ being the x coordinate. To correct for the linearity of the model, a modified thrust coefficient $\widetilde{C_T} = 2\left(1 - \sqrt{1 - C_T}\right)$ is used. A wake-loss correction, obtained from a Jensen model[56] with expansion coefficient 0.04, has been used to calculate the actual force magnitude imposed by each rotor. Furthermore, to account for the solid boundary of the wind tunnel floor, all turbines are mirrored at the plane $\tilde{z} = 0$.

In Figure 11, the present results are compared to the model given in Equation (2).[29] The model assumes uniform incoming flow. However, since the present results are from an evolving boundary layer, the values have been normalized to the undisturbed flow, U_{clean}, at the same position rather than the free-stream velocity. The model was proposed to be valid only upstream of $x/D = -2$, and as such, only values upstream of this point are shown in the figure. There is scatter in the results, nevertheless, the model consistently underpredicts the velocity deficit for both farm layouts and both ADs and turbines by approximately 1% (see Figure 11). The deviations might come from the non-uniform inflow conditions in the experiments or any small confinement effects in the wind tunnel. Earlier lab-scale works report that the global induction is about 1% stronger in a boundary layer[50] than in a uniform flow.[17] This trend agrees with the current results and indicates that the influence of the boundary layer

is significant. In full-scale wind farms, the magnitude of the induction depends on the ABL conditions.[27] With regards to that, Equation (2) predicts the global induction reasonably well.

3.2 | Wake region

The wakes of the porous disk and the model wind turbine were examined in detail by Helvig et al.[46] However, their measurements were performed in a uniform flow and with a smaller field of view. In addition, the presence of another WGO in the wake of the first one has not been studied. It is therefore interesting to make a short comparison between the wakes in this work.

Profiles of the streamwise velocity in the wake of the leading WGOs are shown in Figure 12. In the near wake, there are only minor differences between the different farm layouts. In contrast, the far wakes show dependence on the layouts, as wakes of other turbines or ADs start to protrude into the measurement plane for some of the incoming flow angles. It is thus hard to make a direct comparison between all the farms. Therefore, the analysis is limited to the 0° cases. They serve as the extreme cases, with the second row WGO being centered in the measurement plane for the aligned case, and with the second row WGO being located at the maximum 2.5D away from the measurement plane for the staggered cases.

The near wake of the leading row turbine is stronger in the top half, while the wake of the AD is marginally stronger for the bottom half. However, beneath the bottom tip, the velocity is significantly higher for the turbine. These differences persist throughout the measurement domain for the staggered farms, albeit with a reduced magnitude. The velocity deficit in the AD and wind turbine wakes approach each other, such that only minor differences are seen at $x/D = 8$. Due to the effect of the second row WGO, this can only be observed for the staggered cases. The differences below the bottom tip of the WGOs persist longer. For the aligned cases, the induction of the second row WGO, located at $x/D = 5$, is evident in the profiles at $x/D = 4.75$. As with the leading WGO, the upstream induction is larger for the AD. In the same way as downstream of the leading WGO, the wake of the turbine is stronger than the AD wake downstream of the second row WGO, seen in the profiles at $x/D = 6.5$. This time, however, the difference lies in the center of the wake. Also, the velocity reduction below the bottom tip is higher for the AD. The wake profiles homogenize more rapidly downstream of the second WGOs, but the difference in the flow beneath the bottom tips

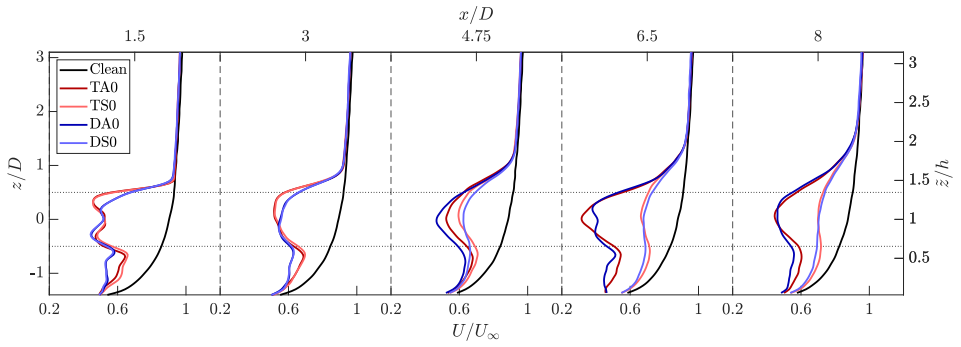

FIGURE 12 Profiles of the streamwise velocity downstream of the leading wake generating object. Only the 0° cases are shown.

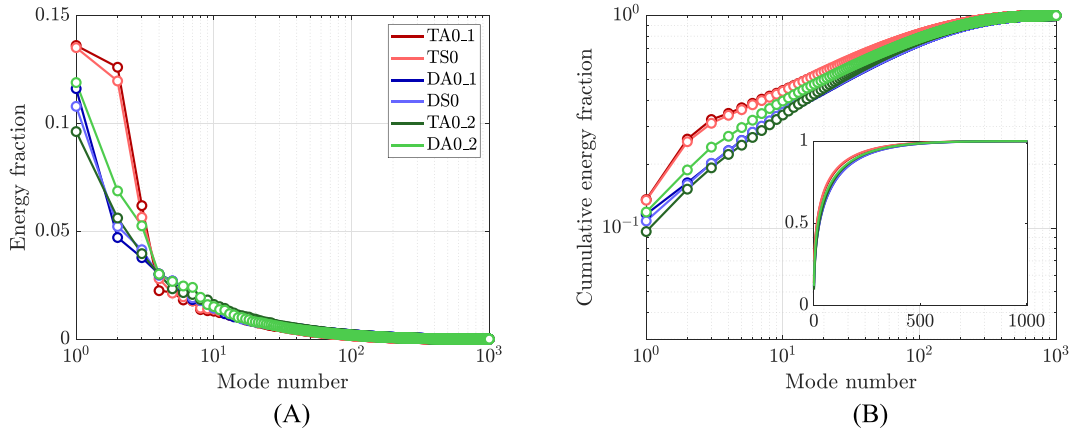

FIGURE 13 (A) Energy fraction of POD modes and (B) cumulative energy fraction of POD modes. The data plotted in green are for an interrogation window downstream of the second row wake generating object.

persists farther downstream. The reduced velocity of the flow beneath the tips for the AD cases can be an effect of the tower. The expected global rotation of the flow downstream of a wind turbine would move the effect of the turbine tower out of the measurement plane, which explains the higher velocity for the turbine cases. In sum, the induction is higher for the disks, and the wakes are stronger for the turbines. From this, it can be seen that the drag, or thrust, of a WGO cannot be determined directly from two-dimensional induction or wake integration.

Downstream of the first WGO, at $x/D = 1.5$, all velocity profiles have two minima, one in the top half and one in the bottom half of the wake. The magnitude of the minima varies between the AD and turbine cases, as described in the previous paragraph. At the same downstream distance from the second WGO, for the aligned cases, the two minima only exist in the AD wake, while the turbine wake has a larger, centered minimum. Thus, the different wakes of the leading WGOs impact the second row WGO in distinct ways (although unknown differences in the rotational speed of the turbines might also influence the wake). To further evaluate this, it is interesting to perform a modal decomposition to evaluate the structures in the flow. For this purpose, snapshot proper orthogonal decomposition (POD), developed by Sirovich,[57] has been applied. Every instantaneous velocity fluctuation field is viewed as a snapshot $\mathbf{u}_n$, which is decomposed into modes $\boldsymbol{\phi}_i$. Every mode has a corresponding energy

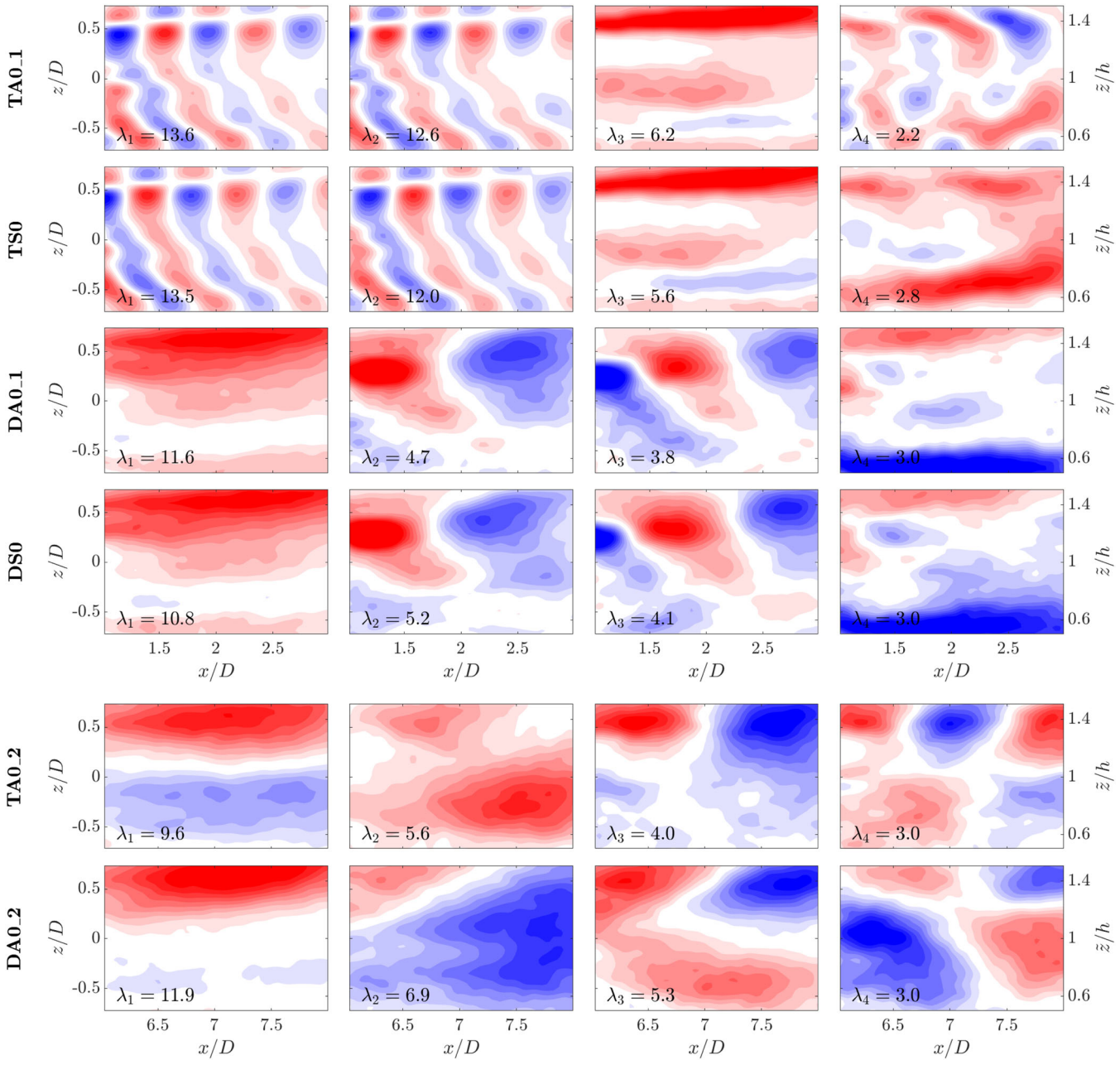

FIGURE 14 The streamwise component of the first four modes of the 0° cases. The last two rows are for the modes downstream of the second row wake generating object.

value, namely, λ_i, and it is possible to order modes by their energy content with $i = 1$ being the first mode with the highest energy. The most energetic modes thus contain the most energetic spatial structures in the flow. The modes are related to the snapshots through

$$\mathbf{u}_n = \sum_{n=1}^{N} A_i^n \boldsymbol{\phi}_i, \tag{3}$$

where A is a coefficient matrix and N is the number of snapshots or instantaneous velocity fields.

For the wake region, snapshot POD was performed on a limited field of interest in the wake of the leading and second row WGOs. The field stretches from 1D to 3D downstream of the WGOs. For the second row WGOs, the limits are then 6D and 8D; recall the second turbine is located at 5D. Vertically, the interrogation window is limited to $-0.75 \le z/D \le 0.75$. The energy content of the modes is shown in Figure 13. For the aligned case, a 1 or 2 is appended to the case name for the wake of the leading and second row WGOs, respectively. The first couple of modes downstream of the leading turbine display the highest energy content, while the corresponding modes downstream of the second row turbine have lower energy content. In fact, the energy content of the modes downstream of the second row turbine is similar to the energy content in the modes downstream of the leading AD. For the second row AD, the energy content is slightly higher than for the leading AD. It is interesting to note that the wake of the leading WGO has a different effect on the energy content of the second row WGO depending on whether it is an AD, which yields a higher energy content, or turbine, which yields a lower energy content.

To further understand the structures, it is also possible to look at the modes themselves. The streamwise component of the first four modes for each of the six POD cases are shown in Figure 14. The first two modes of the leading turbine wake are dominated by structures in the top shear layer of the wake, that is, tip vortices. The tip vortices in the bottom of the interrogation window are also clear, but weaker than the top. This is possibly an effect of the tower or the higher shear and turbulence intensity in this region. In agreement with previous results, the tip vortices are not present in the AD wakes.[46] The large structures in the most energetic mode of the disk wake are similar, although not identical, to the third mode of the leading wind turbine wake. The next modes in the AD wakes contain gradually smaller structures. This is in accordance with many turbulent flows without periodicity, where the large structures carry most of the energy. It can be compared to the classical spectra of velocity fluctuations, where the same behavior is observed.

The four displayed modes of the wake of the second row turbine do not show any trace of the tip vortices. The turbulent inflow in the wake from the leading turbine leads to faster breakdown of the vortices. Instead, the modes are more similar to the modes of the second row AD, and are also more like the modes downstream of the leading disks. The instantaneous swirling strength in Figure 15 illustrates how the tip vortices are much stronger downstream of the first turbine than the second. Earlier works have shown that tip vortices are less prominent after 10 rows of turbines[58] and, indeed, already after the second turbine.[18] The similarity between the first four modes in the wakes of the second row WGOs show that the main turbulent structures, and therefore some of the transport mechanisms, in the flow are similar. This is important, because even though earlier works have shown that the energy entrainment mechanism is changed by the lack of tip vortices in the wake of a single AD compared to a wind turbine,[41,46] this difference is reduced already after the second row of WGOs. Thus, an AD might replicate the flow in a wind farm better than they do for a single turbine. This is a significant result, as it shows that wind farm modeling can be performed by simple, nonrotating models, with a smaller impact on the results than expected from single WGO comparisons.

The inflow to any downstream turbine is turbulent, yielding higher turbulent mixing. This leads to enhanced transition to the far wake.[59] The modal decomposition shows that the turbulence in the wind farm does not get more complicated after the second row of WGOs. Instead, the signature of the WGO becomes less prominent. The reduction of the size of the structures with increasing mode number is an indication of the turbulent cascade, although a general influence of the WGO is still visible.

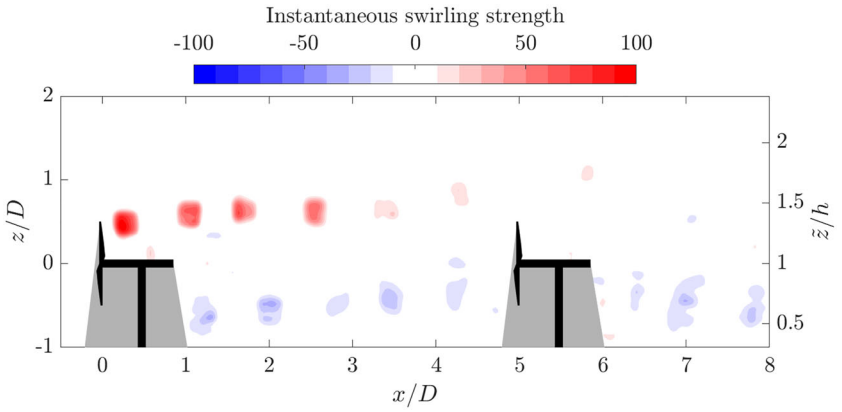

FIGURE 15 Instantaneous swirling strength for TA0.

3.3 | Entrainment region

Entrainment of energy from the flow above a wind farm is important to facilitate wake recovery and thus give power to downstream turbines. One important factor for the entrainment of mean kinetic energy (MKE) is the transport by turbulent fluctuations.[33,41,60,61] Mathematically, it is formulated as $-U\overline{u'w'}/U_\infty^3$. The negative sign ensures that positive values represent downward transport of energy. Figure 16A shows the turbulent transport of MKE at several heights above the WGOs, as well as at the bottom tip of the WGOs. The highest position is at 1D above the top of the farm. Since the measurements are done in the entrance region of the farm, the flow above this height is not likely to be significantly affected. Indeed, at $z/D = 1.5$, the farm cases only deviate from the clean case at the rear end of the field of view. Between $z/D = 0.5$ and $z/D = 1$, the turbulent transport is higher for the turbine cases than for the AD cases. In the most extreme case, at $z/D = 0.75$, the magnitude is almost twice as high for the turbine. Also, from below, there is stronger entrainment in the turbine cases.

In addition to the entrainment by the fluctuations, it is also important to consider the downward transport of MKE by the mean vertical velocity. In particular, the mean vertical velocity has significant magnitude in the developing region near the beginning of the farm. Therefore,

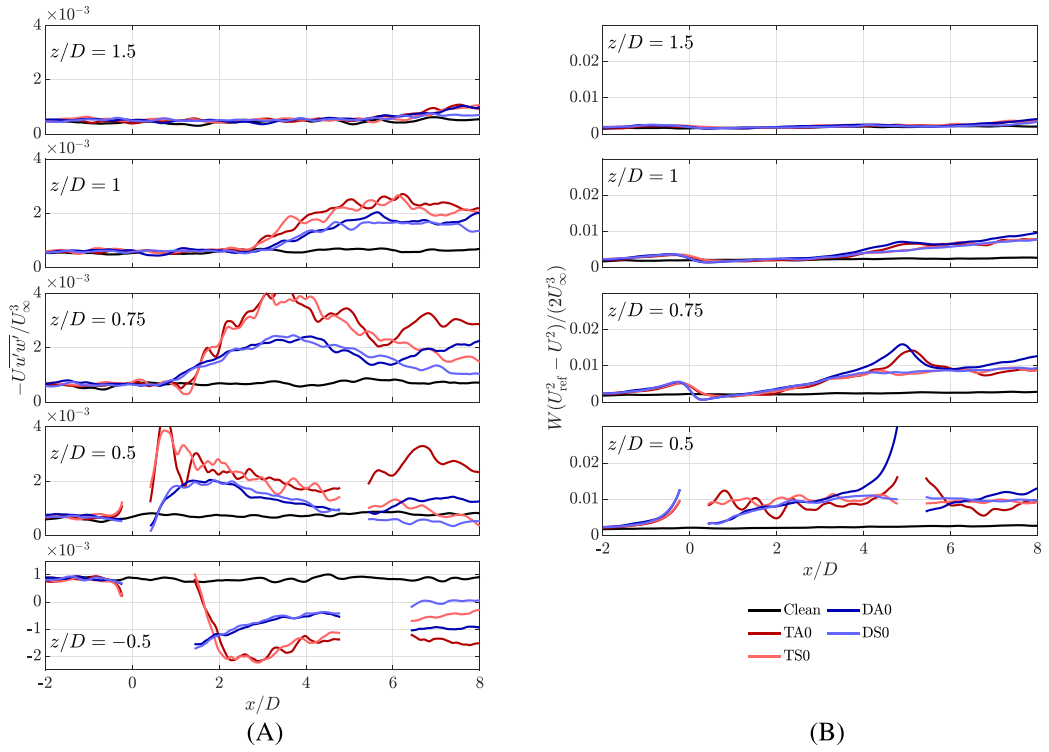

FIGURE 16 Transport of (A) mean kinetic energy by turbulent fluctuations and (B) mean vertical velocity in the entrainment region over the first rows of the farm. Note the different scales in (A) and (B).

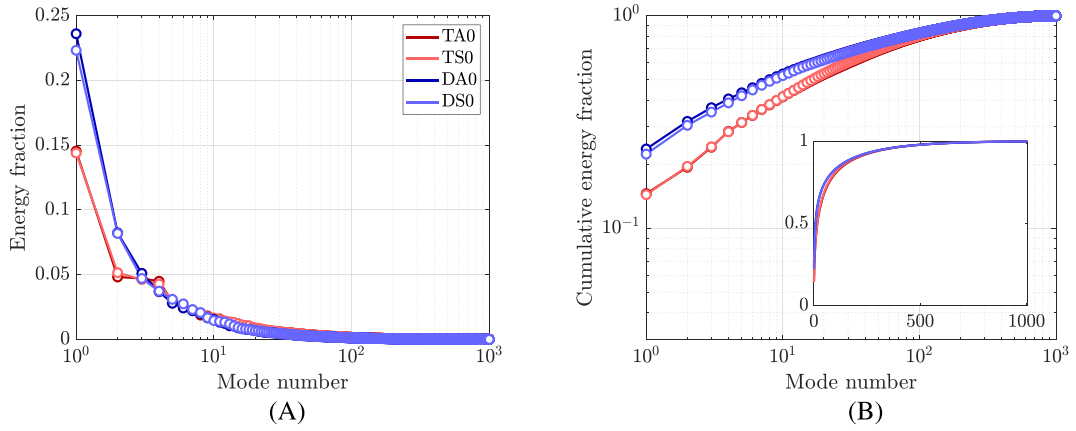

FIGURE 17 (A) Energy fraction of POD modes and (B) cumulative energy fraction of POD modes.

Figure 16B shows $W(U_{ref}^2 - U^2)/2$, where U_{ref} is the undisturbed streamwise velocity at $z/D = 3$. As expected, and also shown by, for example, Cortina et al.[34] and Segalini and Chericoni,[18] mean transport plays a bigger role than turbulent transport of MKE into the entrance region of the farm (note the different scales of Figure 16A,B). The difference is more pronounced in this work than in Segalini and Chericoni,[18] with the transport by the mean velocity being almost an order of magnitude larger. The results are not directly comparable to Segalini and Chericoni's,[18] as they calculate the spanwise average over a farm, including the flow between columns of turbines, while the present results only see the flow directly above a column. There are only minor differences between the values of the turbine and AD cases (although the differences are as large as the magnitude of the turbulent transport). Just downstream of the WGOs, at $z/D = 0.5$, the transport is higher for the turbines than the ADs. The transport by the mean velocity from below the turbines has not been calculated, as there is no well defined reference velocity at this position. In all cases, there is net transport of energy into the wake region.

As the transport of MKE is dominated by the mean flow in the entrance region, the differences in the turbulent fluctuations have less impact in the comparison between ADs and turbines. However, in large farms, this difference balances, and sufficiently far downstream, the turbulent transport dominates.[18,34] In fact, for an infinite farm, only the turbulent transport is present, as there is no mean vertical velocity in the fully

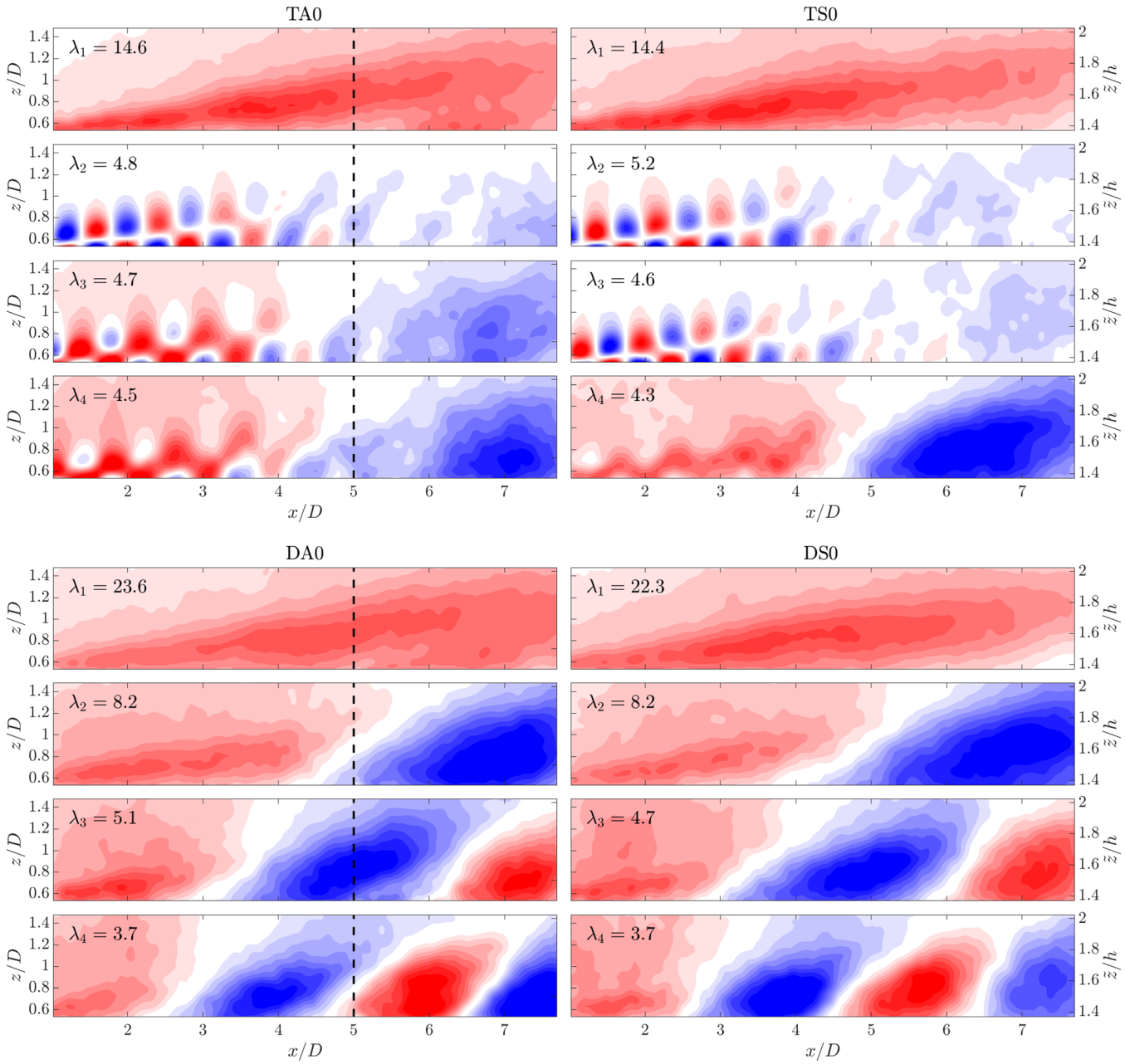

FIGURE 18 The streamwise component of the first four modes in the entrainment region of the 0° cases. The dashed vertical line shows the position of the second row WGO for the aligned cases.

developed flow.[18] Therefore, the differences in $-U\overline{u'w'}$ are still important when using ADs in large wind farms. Further studies are needed to evaluate these parameters farther downstream in wind farms consisting of turbines and ADs.

In the same manner as in the wake region, snapshot POD has been performed on an interrogation window covering the entrainment region. The field of view is limited by $0.5 \le x/D \le 8$ and $0.5 \le z/D \le 1.5$. In contrast with the energy content of the modes in the wake region, Figure 17 shows that the first modes of the AD cases are more energetic than the first modes of the turbine cases in the entrainment region. In particular, the two first modes show higher energy content. For the turbine cases, Modes 2 and 3 have similar energy content, in the same way as the two first modes have in the wake region.

Figure 18 shows the streamwise component of the first four modes for the 0° cases. It is interesting to note that the farm layout does not have a major impact on the flow structures, that is, the modes of the aligned and staggered cases do not differ significantly. The first mode is similar for the four cases, and it is dominated by a single structure spanning from the top of the leading WGO. Since the sign is the same for the entire interrogation window, this mode represents turbulent structures larger than the field of view. If the energy fraction of the first mode is multiplied with the integrated turbulent kinetic energy (k_{2D}) in the POD interrogation window, the energy content becomes similar for the first mode of the different cases, with a value of around $k_{2D}\lambda_1 = 8.3$ for the AD farms and a value of approximately $k_{2D}\lambda_1 = 9.5$ for the turbine cases. This value is a quantification of the turbulent energy carried by the first mode, and since it has similar values for the ADs and turbines, it shows that the turbulent structures with a scale larger than the interrogation window are not significantly affected by the type of WGO. For the AD cases, the next couple of modes show structures of decreasing size. This corresponds to a regular turbulent spectrum, where the larger wave numbers carry most of the energy and smaller structures contain a decreasing amount of energy. For the turbine cases, Modes 2 and 3 are dominated by small, periodic structures. These are ascribed to the tip vortices also seen in Figure 15. As in that figure, there are no traces of tip vortices downstream of the second row turbine in the aligned farm. This confirms that the flow downstream of the second row WGO is less dependent on the type of WGO used to model the wind turbines and that it is justifiable to use static models in wind farm modeling. A general breakdown to smaller structures can be observed in the fourth mode, although traces of the tip vortices can be seen even here. This mode is somewhat similar to the second mode of the disk cases. The higher integrated TKE in the turbine cases and the observed tip vortices are the main differences between the disk and turbine farms, whereas the first mode is relatively unaffected by the WGOs.

4 | CONCLUSION

An experimental study on the flow upstream and in the entrance region of wind farms in aligned and staggered layouts has been presented. The main focus has been on the differences between the farm made of rotating wind turbine models and static wind turbine models (ADs). Through two-dimensional, two-component PIV, the total field of view covered 20 rotor diameters in the streamwise direction and 4.5 rotor diameters in the vertical direction.

The results confirm that the global induction, or wind farm blockage, exists and is measurable. However, it is not significantly different between different farm layouts, nor between ADs and rotating models. Compared to Segalini's[29] model, the measured induction is higher than predicted but within 2% of the undisturbed velocity. The local induction for the leading WGO, however, differs between the AD and turbine cases, with a higher induction measured for the ADs. This difference is seen from $x/D = -1.5$ and closer. In contrast, the wake downstream of a turbine has a higher total velocity deficit than the wake downstream of a disk, both for the first and second row turbine in the aligned farm. Energy entrainment by the mean velocity is approximately the same for the different WGOs. However, transport by turbulence is higher for the turbine case, although with a much smaller magnitude than transport by the mean. Far downstream in a wind farm, it is expected that the turbulent transport dominates,[18] and as such, this is an important difference between the WGOs.

The present results only show the flow around the two first rows of WGOs. However, the turbulent wake of the leading WGO reduces the length of the near wake of the second row WGO. The tip vortices are not visible in the second wake, which is in agreement with the findings of Segalini and Chericoni.[18] Instead, the structures in the wake of the second row AD and turbine are similar. In addition, it has been shown that the largest turbulent structures in the entrainment region are unaffected by the type of WGO. In sum, this shows that ADs reproduce the flow in and around a wind farm better than a single AD reproduces the flow around a single turbine. Nonetheless, the ADs and rotating turbines produce discernibly different results and thus care should be taken when estimating induction with, for instance, RANS employing ADs.

ACKNOWLEDGEMENTS

The authors acknowledge and thank Sanne de Jong Helvig for her assistance in preparing the experimental equipment and setup. A.S. is supported by the Swedish strategic research program STandUP for Wind.

PEER REVIEW

The peer review history for this article is available at https://www.webofscience.com/api/gateway/wos/peer-review/10.1002/we.2855.

DATA AVAILABILITY STATEMENT

Data published in article are available in the NTNU Open Research Data repository at https://doi.org/10.18710/RDPXQL.

ORCID

Magnus K. Vinnes https://orcid.org/0000-0003-0980-1827
Nicholas A. Worth https://orcid.org/0000-0002-7084-9304
Antonio Segalini https://orcid.org/0000-0001-8667-0520
R. Jason Hearst https://orcid.org/0000-0003-2002-8644

REFERENCES

1. Manwell JF, McGowan JG, Rogers AL. *Wind Energy Explained*. John Wiley & Sons, Ltd; 2009.
2. Stevens RJAM, Gayme DF, Meneveau C. Large eddy simulation studies of the effects of alignment and wind farm length. *J Renew Sustain Energy*. 2014;6(2):23105. doi:10.1063/1.4869568
3. VerHulst C, Meneveau C. Altering kinetic energy entrainment in large eddy simulations of large wind farms using unconventional wind turbine actuator forcing. *Energies*. 2015;8(1):370-386. doi:10.3390/en8010370
4. Allaerts D, Meyers J. Gravity waves and wind-farm efficiency in neutral and stable conditions. *Bound-Layer Meteorol*. 2018;166(2):269-299.
5. Gadde SN, Stevens RJAM. Interaction between low-level jets and wind farms in a stable atmospheric boundary layer. *Phys Rev Fluids*. 2021;6(1):14603. doi:10.1103/PhysRevFluids.6.014603
6. España G, Aubrun S, Loyer S, Devinant P. Spatial study of the wake meandering using modelled wind turbines in a wind tunnel. *Wind Energy*. 2011;14(7):923-937. doi:10.1002/we.515
7. España G, Aubrun S, Loyer S, Devinant P. Wind tunnel study of the wake meandering downstream of a modelled wind turbine as an effect of large scale turbulent eddies. *J Wind Eng Industr Aerodyn*. 2012;101:24-33. doi:10.1016/j.jweia.2011.10.011
8. Howland MF, Bossuyt J, Martínez-Tossas LA, Meyers J, Meneveau C. Wake structure in actuator disk models of wind turbines in yaw under uniform inflow conditions. *J Renew Sustain Energy*. 2016;8(4):43301. doi:10.1063/1.4955091
9. Yu W, Hong VW, Ferreira C, Van Kuik GMA. Experimental analysis on the dynamic wake of an actuator disc undergoing transient loads. *Experiments Fluids*. 2017;58:149. doi:10.1007/s00348-017-2432-9
10. Abdulrahim A, Akpolat MT, Hassanein A, Perçin M, Uzol O. Effects of inflow boundary layer on the wake of a radially non-uniform porous disk. *J Renew Sustain Energy*. 2021;13(3):33302. doi:10.1063/5.0045404
11. Travis KN, Smith SE, Vignal L, et al. Characterization of coupling between inertial particles and turbulent wakes from porous disk generators. *J Fluid Mech*. 2022;933:A42. doi:10.1017/jfm.2021.1095
12. Theunissen R, Housley P, Allen CB, Carey C. Experimental verification of computational predictions in power generation variation with layout of offshore wind farms. *Wind Energy*. 2015;18(10):1739-1757. doi:10.1002/we.1788
13. Bossuyt J, Howland MF, Meneveau C, Meyers J. Measurement of unsteady loading and power output variability in a micro wind farm model in a wind tunnel. *Exper Fluids*. 2017;58(1):1-17. doi:10.1007/s00348-016-2278-6
14. Bastankhah M, Porté-Agel F. Wind tunnel study of the wind turbine interaction with a boundary-layer flow: upwind region, turbine performance, and wake region. *Phys Fluids*. 2017;26(6):65105. doi:10.1063/1.4984078
15. Li L, Hearst RJ, Ferreira MA, Ganapathisubramani B. The near-field of a lab-scale wind turbine in tailored turbulent shear flows. *Renew Energy*. 2020;149:735-748. doi:10.1016/j.renene.2019.12.049
16. Neunaber I, Hölling M, Stevens RJAM, Schepers G, Peinke J. Distinct turbulent regions in the wake of a wind turbine and their inflow-dependent locations: the creation of a wake map. *Energies*. 2020;13(20):5392. doi:10.3390/en13205392
17. Segalini A, Dahlberg JÅ. Blockage effects in wind farms. *Wind Energy*. 2020;23(2):120-128. doi:10.1002/we.2413
18. Segalini A, Chericoni M. Boundary-layer evolution over long wind farms. *J Fluid Mech*. 2021;925:A2. doi:10.1017/jfm.2021.629
19. Porté-Agel F, Bastankhah M, Shamsoddin S. Wind-turbine and wind-farm flows: a review. *Bound-Layer Meteorol*. 2020;174(1):1-59. doi:10.1007/s10546-019-00473-0
20. Vermeer LJ, Sørensen JN, Crespo A. Wind turbine wake aerodynamics. *Progress Aerosp Sci*. 2003;39(6–7):467-510. doi:10.1016/S0376-0421(03)00078-2
21. Vinnes MK, Gambuzza S, Ganapathisubramani B, Jason Hearst R. The far wake of porous disks and a model wind turbine: similarities and differences assessed by hot-wire anemometry. *J Renew Sustain Energy*. 2022;14:23304. doi:10.1063/5.0074218
22. Medici D, Ivanell S, Dahlberg JÅ, Alfredsson PH. The upstream flow of a wind turbine: blockage effect. *Wind Energy*. 2011;14(5):691-697. doi:10.1002/we.451
23. Howard KB, Guala M. Upwind preview to a horizontal axis wind turbine: a wind tunnel and field-scale study. *Wind Energy*. 2016;19(8):1371-1389. doi:10.1002/we.1901
24. Simley E, Angelou N, Mikkelsen T, Sjöholm M, Mann J, Pao LY. Characterization of wind velocities in the upstream induction zone of a wind turbine using scanning continuous-wave lidars. *J Renew Sustain Energy*. 2016;8(1):13301. doi:10.1063/1.4940025
25. Troldborg N, Meyer Forsting AR. A simple model of the wind turbine induction zone derived from numerical simulations. *Wind Energy*. 2017;20(12):2011-2020. doi:10.1002/we.2137
26. Bleeg J, Purcell M, Ruisi R, Traiger E. Wind farm blockage and the consequences of neglecting its impact on energy production. *Energies*. 2018;11(6):1609. doi:10.3390/en11061609
27. Schneemann J, Theuer F, Rott A, Dörenkämper M, Kühn M. Offshore wind farm global blockage measured with scanning lidar. *Wind Energy Sci*. 2021;6(2):521-538. doi:10.5194/wes-6-521-2021
28. Branlard E, Meyer Forsting AR. Assessing the blockage effect of wind turbines and wind farms using an analytical vortex model. *Wind Energy*. 2020;23:2068-2086. doi:10.1002/we.2546
29. Segalini A. An analytical model of wind-farm blockage. *J Renew Sustain Energy*. 2021;13:33307. doi:10.1063/5.0046680

30. Newman J, Lebron J, Meneveau C, Castillo L. Streamwise development of the wind turbine boundary layer over a model wind turbine array. *Phys Fluids*. 2013;25(8):85108. doi:10.1063/1.4818451
31. Newman AJ, Drew DA, Castillo L. Pseudo spectral analysis of the energy entrainment in a scaled down wind farm. *Renew Energy*. 2014;70:129-141. doi:10.1016/j.renene.2014.02.003
32. Hamilton N, Melius M, Cal RB. Wind turbine boundary layer arrays for Cartesian and staggered configurations—Part I, flow field and power measurements. *Wind Energy*. 2015;18(2):277-295. doi:10.1002/we.1697
33. Cortina G, Calaf M, Cal RB. Distribution of mean kinetic energy around an isolated wind turbine and a characteristic wind turbine of a very large wind farm. *Phys Rev Fluids*. 2016;1(7):74402. doi:10.1103/PhysRevFluids.1.074402
34. Cortina G, Sharma V, Torres R, Calaf M. Mean kinetic energy distribution in finite-size wind farms: a function of turbines' arrangement. *Renew Energy*. 2020;148:585-599. doi:10.1016/j.renene.2019.10.148
35. Wu Y-T, Porté-Agel F. Simulation of turbulent flow inside and above wind farms: model validation and layout effects. *Bound-Layer Meteorol*. 2013;146:181-205. doi:10.1007/s10546-012-9757-y
36. Martínez-Tossas LA, Churchfield MJ, Leonardi S. Large eddy simulations of the flow past wind turbines: actuator line and disk modeling. *Wind Energy*. 2015;18(6):1047-1060. doi:10.1002/we.1747
37. Simisiroglou N, Breton S-P, Ivanell S. Validation of the actuator disc approach using small-scale model wind turbines. *Wind Energy Sci*. 2017;2(2):587-601. doi:10.5194/wes-2-587-2017
38. Stevens RJAM, Martínez-Tossas LA, Meneveau C. Comparison of wind farm large eddy simulations using actuator disk and actuator line models with wind tunnel experiments. *Renew Energy*. 2018;116:470-478. doi:10.1016/j.renene.2017.08.072
39. Dong G, Li Z, Qin J, Yang X. Predictive capability of actuator disk models for wakes of different wind turbine designs. *Renew Energy*. 2022;188:269-281. doi:10.1016/j.renene.2022.02.034
40. Aubrun S, Loyer S, Hancock PE, Hayden P. Wind turbine wake properties: comparison between a non-rotating simplified wind turbine model and a rotating model. *J Wind Eng Industr Aerodyn*. 2013;120:1-8. doi:10.1016/j.jweia.2013.06.007
41. Lignarolo LEM, Ragni D, Ferreira CJ, Van Bussel GJW. Experimental comparison of a wind-turbine and of an actuator-disc near wake. *J Renew Sustain Energy*. 2016;8(2):23301. doi:10.1063/1.4941926
42. Camp EH, Cal RB. Mean kinetic energy transport and event classification in a model wind turbine array versus an array of porous disks: energy budget and octant analysis. *Phys Rev Fluids*. 2016;1(4):44404. doi:10.1103/PhysRevFluids.1.044404
43. Camp EH, Cal RB. Low-dimensional representations and anisotropy of model rotor versus porous disk wind turbine arrays. *Phys Rev Fluids*. 2019;4(2):24610. doi:10.1103/PhysRevFluids.4.024610
44. Neunaber I, Hölling M, Whale J, Peinke J. Comparison of the turbulence in the wakes of an actuator disc and a model wind turbine by higher order statistics: a wind tunnel study. *Renew Energy*. 2021;179:1650-1662. doi:10.1016/j.renene.2021.08.002
45. Aubrun S, Bastankhah M, Cal RB, et al. Round-robin tests of porous disc models. *J Phys: Conf Ser*. 2019;1256(1):12004. doi:10.1088/1742-6596/1256/1/012004
46. Helvig SJ, Vinnes MK, Segalini A, Worth NA, Hearst RJ. A comparison of lab-scale free rotating wind turbines and actuator disks. *J Wind Eng Industr Aerodyn*. 2021;209:104485. doi:10.1016/j.jweia.2020.104485
47. Medici D, Alfredsson PH. Measurements on a wind turbine wake: 3D effects and bluff body vortex shedding. *Wind Energy*. 2006;9(3):219-236. doi:10.1002/we.156
48. Maeda T, Kamada Y, Murata J, et al. Wind tunnel study on wind and turbulence intensity profiles in wind turbine wake. *J Thermal Sci*. 2011;20(2):127-132. doi:10.1007/s11630-011-0446-9
49. Lignarolo LEM, Ragni D, Krishnaswami C, Chen Q, Simão Ferreira CJ, van Bussel GJW. Experimental analysis of the wake of a horizontal-axis wind-turbine model. *Renew Energy*. 2014;70:31-46. doi:10.1016/j.renene.2014.01.020
50. Ebenhoch R, Muro B, Dahlberg JÅ, Berkesten Hägglund P, Segalini A. A linearized numerical model of wind-farm flows. *Wind Energy*. 2017;20(5):859-875. doi:10.1002/we.2067
51. Newman AJ, Cal RB, Castillo L. Blade number effects in a scaled down wind farm. *Renew Energy*. 2015;81:472-481. doi:10.1016/j.renene.2015.03.013
52. Mühle F, Adaramola MS, Saetran L. The effect of the number of blades on wind turbine wake—a comparison between 2- and 3-bladed rotors. *J Phys: Conf Ser*. 2016;753:32017. doi:10.1088/1742-6596/753/3/032017
53. Koning C. Influence of the propeller on other parts of the airplane structure. *Aerodynamic Theory*. Springer Berlin Heidelberg; 1935:361-430.
54. West GS, Apelt CJ. The effects of tunnel blockage and aspect ratio on the mean flow past a circular cylinder with Reynolds numbers between 10^4 and 10^5. *J Fluid Mech*. 1982;114:361-377. doi:10.1017/S0022112082000202
55. Mücke T, Kleinhans D, Peinke J. Atmospheric turbulence and its influence on the alternating loads on wind turbines. *Wind Energy*. 2011;14(2):301-316. doi:10.1002/we.422
56. Jensen NO. A note on wind generator interaction, Risø National Laboratory; 1983. Tech. rep.
57. Sirovich L. Turbulence and the dynamics of coherent structures Part I: coherent structures. *Quart Appl Math*. 1987;45(3):561-571.
58. Chamorro LP, Porté-Agel F. Turbulent flow inside and above a wind farm: a wind-tunnel study. *Energies*. 2011;4(11):1916-1936. doi:10.3390/en4111916
59. Jin Y, Liu H, Aggarwal R, Singh A, Chamorro LP. Effects of freestream turbulence in a model wind turbine wake. *Energies*. 2016;9(10):830. doi:10.3390/en9100830
60. Cal RB, Lebrón J, Castillo L, Kang HS, Meneveau C. Experimental study of the horizontally averaged flow structure in a model wind-turbine array boundary layer. *J Renew Sustain Energy*. 2010;2(1):13106. doi:10.1063/1.3289735
61. Goit JP, Meyers J. Optimal control of energy extraction in wind-farm boundary layers. *J Fluid Mech*. 2015;768:5-50. doi:10.1017/jfm.2015.70

How to cite this article: Vinnes MK, Worth NA, Segalini A, Hearst RJ. The flow in the induction and entrance regions of lab-scale wind farms. *Wind Energy*. 2023;1-17. doi:10.1002/we.2855